RSC Advances

PAPER

Cite this: *RSC Adv.*, 2021, **11**, 30544

Enhancing the chloramphenicol sensing performance of Cu–MoS_2 nanocomposite-based electrochemical nanosensors: roles of phase composition and copper loading amount†

Nguyen Tuan Anh,‡*[a] Ngo Xuan Dinh,‡[a] Tuyet Nhung Pham,[a] Le Khanh Vinh,[c] Le Minh Tung[d] and Anh-Tuan Le*[ab]

Received 12th August 2021
Accepted 1st September 2021

DOI: 10.1039/d1ra06100c

rsc.li/rsc-advances

The rational design of nanomaterials for electrochemical nanosensors from the perspective of structure–property–performance relationships is a key factor in improving the analytical performance toward residual antibiotics in food. We have investigated the effects of the crystalline phase and copper loading amount on the detection performance of Cu–MoS_2 nanocomposite-based electrochemical sensors for the antibiotic chloramphenicol (CAP). The phase composition and copper loading amount on the MoS_2 nanosheets can be controlled using a facile electrochemical method. Cu and Cu_2O nanoparticle-based electrochemical sensors showed a higher CAP electrochemical sensing performance as compared to CuO nanoparticles due to their higher electrocatalytic activity and conductivity. Moreover, the design of Cu–MoS_2 nanocomposites with appropriate copper loading amounts could significantly improve their electrochemical responses for CAP. Under optimized conditions, Cu–MoS_2 nanocomposite-based electrochemical nanosensor showed a remarkable sensing performance for CAP with an electrochemical sensitivity of 1.74 μA μM^{-1} cm^{-2} and a detection limit of 0.19 μM in the detection range from 0.5–50 μM. These findings provide deeper insight into the effects of nanoelectrode designs on the analytical performance of electrochemical nanosensors.

1. Introduction

In recent years, the design of nanomaterials (NMs)-based electrochemical sensors for developing simple but reliable analytical methods with high sensitivity and selectivity has attracted increasing attention because the unique properties of NMs are beneficial for improving the performance parameters of electrochemical sensors, such as sensitivity, selectivity, stability, repeatability, and processability.[1] The use of NMs as electrochemical sensors has presented extremely promising prospects for improving the analytical performance toward environmental pollutants and food contaminants, especially in electrochemical sensors based on the direct redox process[1,2]. Various types of NMs such as nanoparticles (metal and metal oxide nanoparticles),[3,4] carbonaceous NMs,[5,6] magnetic NMs,[7] quantum dots,[8,9] and two-dimensional (2D) NMs,[10] have been developed for constructing various electrochemical sensors with low detection limits and good signal amplification. In general, the NMs-based electrodes show significant improvement in the conductivity and electron transfer through the interface of the electrode/electrolyte solution, increasing the electrode/electrolyte junction area, as well as providing more active sites for electrochemical reactions and analyte adsorption as compared with conventional electrodes.[1,11] More interestingly, the physicochemical properties of NMs that have decisive effects on the analytical performance of electrochemical sensors, such as electrocatalytic activity, conductivity, and adsorption efficiency, can be flexibly regulated by controlled material synthesis or design processes. As a result, various routes for improving the sensitivity of the NMs-based electrochemical sensor, including controlled synthesis (in terms of size and shape), the design of novel functional nanometric interfaces, the modulation of surface architecture, and hybrid nanostructures fabrication, have also been exploited.[11] Nonetheless, the performance-improving strategies based on deeply understanding the relationships between structure,

[a]*Phenikaa University Nano Institute (PHENA), Phenikaa University, Hanoi 12116, Vietnam. E-mail: dinh.ngoxuan@phenikaa-uni.edu.vn; tuan.leanh@phenikaa-uni.edu.vn; anh.nguyentuan1@phenikaa-uni.edu.vn*

[b]*Faculty of Materials Science and Engineering, Phenikaa University, Hanoi 12116, Vietnam*

[c]*Institute of Physics at Ho Chi Minh City, Vietnam Academy of Science and Technology (VAST), Ho Chi Minh 70000, Vietnam*

[d]*Department of Physics, Tien Giang University, My Tho City, Tien Giang Province, Vietnam*

† Electronic supplementary information (ESI) available. See DOI: 10.1039/d1ra06100c

‡ N. T. Anh and N. X. Dinh contributed equally to this work.

composition, and reactivity of nanomaterials, especially in novel hybrid structures, have rarely been considered. Moreover, the reproducibility of the initial high performance (*e.g.* sensitivity, selectivity, and stability) in the complex detection environments is still a great challenge for NMs-based electrochemical sensing systems.[1,11] Therefore, further efforts are still required in the functional NM designs for developing advanced electrochemical sensors with excellent performance.

Copper, a low-cost transition metal, and its oxides have received significant attention in the scientific community because of their interesting electronic and surface structures, excellent redox, high catalytic activity, as well as antifungal and antifouling properties.[12–15] With such unique properties, copper-based NMs have been widely used in sensors,[16] photocatalysis,[17] and antimicrobial applications.[15] Copper nanoparticles (Cu-NPs) were developed in electrochemical sensors to take advantage of their inherent merits, such as conductivity, excellent redox, and cost-effectiveness in comparison with other noble metal NPs.[16] Cupric oxide nanoparticles (CuO-NPs), as a semiconductor, were used to improve the electrocatalytic activity of graphene-modified electrodes in the electrochemical sensor for the determination of metronidazole.[13] Cuprous oxide nanoparticles (Cu_2O-NPs), as a typical p-type semiconductor, which integrated with rGO for electrochemical detection of dimetridazole, also showed significant improvement in the electrocatalytic activity towards dimetridazole.[18] The current reviews of NMs-based electrochemical sensors for antibiotics have indicated that hybrid structures, especially the 2D NMs-based hybrid structures, are strong candidates in the development of advanced electrochemical sensors.[11,19] MoS_2 nanosheets, with large surface area, excellent chemical, electrochemical stability, and high carrier mobility are a promising platform for hybrid structures.[20] Moreover, with an abundance of low-coordinated surface atoms on plane edges and defect sites, the 2D-MoS_2 structure offers significant benefits for catalytic activities towards the redox process.[10] The designs of novel hybrid structures can take advantage of the inherent properties of the component materials to improve the performance parameters of the electrochemical sensor. For a given nanohybrid-based electrochemical sensor, its performance relies significantly on the designs of appropriate nanostructure for signal amplification, effective catalysis in redox processes, as well as for selective adsorption with the targeted analyte. The changes in the structure, phase composition, size, and component content directly vary the electronic and surface properties of NMs, which strongly affect the electrochemical processes occurring on the electrode surface. Therefore, understanding how the material parameters, such as phase composition, size, and component content influence the electrochemical properties of the nanostructured electrode is crucial in designing high-performance electrochemical nanosensors.

Antibiotics have been known as revolutionary medicines in treating infectious diseases in livestock and humans. However, the overuse of antibiotics in livestock production (the treatment and prevention of diseases and growth promotion) presents a serious food-safety problem, which poses a potential hazard for human health.[21,22] Chloramphenicol (CAP), a phenolic antibiotic, has been banned for use in food-producing animals within the European Union, the United States, and many other countries because its residue in food may accumulate in the human body and cause aplastic anemia, gray baby syndrome, bone marrow suppression, *etc.*[23–26] Due to its low cost and high efficacy, CAP is still used widely. As a result, the development of effective methods for the rapid, accurate, and on-site determination of CAP continues to attract further studies.

For the above reasons, we have studied the effect of phase composition and copper loading amount on the CAP sensing performance of Cu–MoS_2 nanocomposite-based electrochemical nanosensors. Herein, Cu-NPs, CuO-NPs, and Cu_2O-NPs, as well as various copper loading amounts on the 2D-MoS_2 nanosheets were prepared by using a controlled electrochemical synthesis process. In particular, the CAP analytical performance parameters of the proposed NMs-based electrochemical sensors were evaluated and compared in detail based on the perspective of structure–property–performance relationships. The systematic investigation of the electrochemical sensing performance of copper-based NMs (Cu-NPs, CuO-NPs, Cu_2O-NPs) would provide insight into the role of the crystal phase on the electron transfer through the interface of electrode/electrolyte solution and electrode processes. The present study has shown how the copper loading amount on the MoS_2 nanosheets affects the electrochemical response towards CAP, providing further understanding of MoS_2-based hybrid structure designs in high-performance electrochemical sensors.

2. Experimental procedures

2.1. Chemicals and apparatus

Two pure identical copper plates (15 × 2 × 0.5 cm) as two electrodes were used for the electrochemical synthesis. Sodium citrate tribasic dihydrate ($C_6H_5Na_3O_7 \cdot 2H_2O$) and L-ascorbic acid (vitamin C-98%) were obtained from Shanghai Chemical Reagent. Potassium chloride (KCl), sodium chloride (NaCl), dibasic sodium phosphate (Na_2HPO_4), and potassium dihydrogen phosphate (KH_2PO_4) were purchased from Merck KGaA, Germany. Chloramphenicol (CAP > 98%) and MoS_2 (98%, <2 μm) were supplied by Sigma-Aldrich. All of the above chemicals were utilized without any further purification. Carbon screen-printed electrodes (SPEs-DS110) were purchased from DS Dropsens, Spain.

2.2. Fabrication of CuO, Cu, Cu_2O nanomaterials and Cu–MoS_2 nanocomposite-modified SPEs

Cu-NPs, CuO-NPs, and Cu_2O-NPs, as well as various copper loading amounts on the MoS_2 nanosheets, were prepared by using a controlled simple electrochemical synthesis process. The two parallel copper plates as a copper ion creation source were put into a 250 mL glass beaker filled with an electrolyte consisting of sodium citrate in the presence of L-ascorbic acid. The Cu–MoS_2 nanocomposites were prepared by the same method with a slight modification. Before the electrolysis process, 10 mL of MoS_2 nanosheets suspension with a concentration of 2 mg mL^{-1} was added to an electrolyte solution.

Subsequently, a direct current (DC) voltage source was supplied to the electrodes at room temperature and under magnetic stirring. In this experiment, four parameters, namely, the concentrations of sodium citrate and L-ascorbic acid, reaction time, and applied DC voltage had profound effects on the obtained products (see the ESI S1 Experiments† for more details).

All SPE-based electrodes modified with CuO-NPs, Cu-NPs, Cu_2O-NPs, and Cu–MoS_2 nanocomposites were prepared *via* a facile dropping method. Firstly, all SPEs were polished using a 0.05 μm alumina slurry, then washed several times with deionized water and ethanol, and dried at room temperature. Finally, the solutions of prepared NMs were dropped onto the surface of the working electrode, naturally air-dried, and stored at room temperature for further electrochemical experiments.

2.3. Preparation of real samples

Milk and honey samples were purchased from the local supermarket. To prepare milk samples, 1 mL of milk in 5 mL of PBS (0.1 M) was spiked with various known amounts of CAP standard and the resulting solution was mixed completely by a vortex mixer. For the honey sample preparation, 1 g of honey was dissolved in 5 mL PBS (0.1 M) and transferred to a microcentrifuge tube. The solution was centrifuged for 5 min and filtered through a filter paper. Finally, the different known amounts (5, 10, and 20 μM) of CAP standard were added.

2.4. Characterization techniques

The UV-vis absorbance spectra were recorded (HP 8453 spectrophotometer) within the wavelength range of 400 to 800 nm. The crystalline structures of the samples were analyzed by X-ray diffraction using Cu Kα radiation (λ = 0.154056 nm). The Raman spectra were collected with a MacroRAM, Horiba using a 785 nm excitation laser source. The pH measurements were recorded with a Benchtop pH Meter (Laqua pH 1200) with a glass working electrode.

2.5. Electrochemical measurements

All electrochemical measurements were conducted with an electrochemical workstation (Palmsens 4, PS Trace, PalmSens, The Netherlands). To characterize the electrochemical properties of the electrodes, cyclic voltammetry (CV) was performed by applying a potential range of 0.6 to −0.2 V in 0.1 M KCl solution containing 5 mM $K_3[Fe(CN)_6]/K_4[Fe(CN)_6]$ at a scan rate of a 50 mV s^{-1}. The electrochemical behavior of CAP on the modified SPE with various materials was investigated using CV and differential pulse voltammetry (DPV) measurements in aqueous phosphate buffer electrolyte solution (0.1 M PBS). The CV measurement was conducted for investigating the effect of scan rate in the potential range between −1 and 0 V, $T_{equilibrium}$ = 60 s. The DPV measurements were completed under the following conditions: scan rate of 6 mV s^{-1}, $T_{equilibrium}$ = 60 s, E_{pulse} = 0.075 V, T_{pulse} = 0.2 s in the potential range of −0.4 to −0.8 V. All measurements were conducted at room temperature (25 ± 2 °C).

3. Results and discussion

3.1. Characterization of Cu-based nanomaterials and Cu–MoS_2 nanocomposites

To investigate the effect of phase composition on the CAP electrochemical sensing performance, Cu-NPs, CuO-NPs, and Cu_2O-NPs were prepared by using a simple electrochemical method through changing the concentration of sodium citrate and L-ascorbic acid (see ESI S1 Experiments† for more details). Under the same conditions of reaction time and applied electrolysis voltage, CuO-NPs were obtained with sodium citrate and ascorbic acid at 0.5 g L^{-1} concentration, while the formation of Cu_2O-NPs occurred at higher concentrations of 0.75 g L^{-1} and 1 g L^{-1} for sodium citrate and ascorbic acid, respectively. Cu-NPs were also formed at 0.75 g L^{-1} sodium citrate and 2 g L^{-1} ascorbic acid in the electrolyte solution. The UV-vis absorption spectra of Cu-NPs, CuO-NPs, and Cu_2O-NPs are presented in Fig. 1a. The presence of characteristic peaks at 460, 585, and 690 nm corresponding to Cu_2O-NPs, Cu-NPs, and CuO-NPs shows that various copper phase compositions were successfully designed.

To further confirm the formation of the obtained Cu-based NMs with different and tunable phase compositions by the electrochemical method, X-ray diffraction (XRD) studies of three samples were performed under various synthesis conditions as shown in Fig. 1b. For the CuO sample, the diffraction

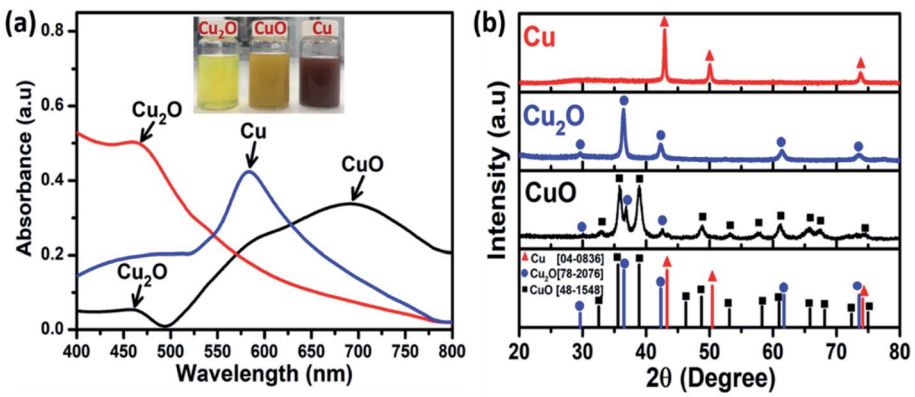

Fig. 1 UV-vis spectra (a) and X-ray diffraction patterns (b) of Cu-based NMs. Inset images show changes in the colors of the reaction mixtures.

peaks (black line) at $2\theta = 32.8°$, 35.6°, 38.7°, 48.8°, 53.4°, 61.3°, 65.8°, and 67.5° coincided with the diffraction planes of (110), (002), (111), (202), (020), (113), (022), and (310) planes of tenorite, respectively, and matched the Joint Committee on Powder Diffraction Standards (JCPDS), card no. 48-1548. However, the Cu_2O impurity phase was present in an insignificant amount, which was consistent with the UV-vis results. For the Cu_2O sample (blue line), all the diffraction peaks in the XRD pattern at 2θ values of 29.2°, 36.1° 41.9°, 61.1°, and 73.1° correspond to the planes of (110), (111), (200), (220), and (311) of cuprite. These patterns were consistent with the database JCPDS card no. 78-2076. In the XRD pattern of the Cu sample (red line), Bragg's reflections were observed at 2θ values of 42.9°, 50.1°, and 73.8°, representing the (111), (220), and (200) planes of face-centered-cubic (fcc) copper, respectively, in agreement with the JCPDS card no. 78-2076. Interestingly, as can be seen from Fig. 1b, no additional peaks related to impurities were observed, indicating the high crystallinity of the formed Cu_2O-NPs and Cu-NPs, in good agreement with the UV-vis results.

Raman spectroscopy is a powerful method for the identification of the oxidation state of copper.[27] The Raman spectra of Cu-NPs, Cu_2O-NPs, and CuO-NPs are shown in Fig. S2;† the Cu-NPs and Cu_2O-NPs have high phase purity and no unintended phases such as $Cu(OH)_2$ and CuO. Based on previous reports,[28–30] the observed Raman bands of Cu_2O may be assigned as lattice modes at about 110 cm^{-1} (E_u), 325 cm^{-1} (A_{2u}), 620 cm^{-1} (T_{1u} TO, LO), and in the vicinity of 525 cm^{-1} for the only Raman-active T_{2g} mode. The bands at 225 cm^{-1} ($2E_u$), in the range between 400 and 490 cm^{-1}, and at 690 cm^{-1} were assigned to multiphonon Raman scattering.[28,31] An additional feature at 180 cm^{-1} is a resonant gap mode due to the local vibrations of Cu on O-sites.[28,31,32] In the case of CuO-NPs, the Raman spectra show three optical vibrational modes at 289 cm^{-1} (A_g), 355 cm^{-1} (B_{1g}), and 633 cm^{-1} (B_{2g}).[27,33] However, in addition to CuO peaks, Cu_2O peaks can also be seen, which indicate the coexistence of both CuO and Cu_2O phases in the prepared CuO-NPs sample. These results are consistent with the obtained UV-vis and XRD results. Thus, it can be concluded that the proposed electrochemical method was efficient for the design of Cu-based NMs with various phase compositions. This is critical to the design of appropriate nanostructures for improving the performance parameters of the electrochemical sensors.

To investigate the effect of the copper loading amount on the MoS_2 nanosheets on the CAP electrochemical sensing performance, Cu–MoS_2 nanocomposites with various copper loading amounts were prepared by varying the electrochemical reaction time. Fig. 2a shows the UV-vis spectra of Cu–MoS_2 nanocomposites synthesized at different reaction times starting from 30 min to 90 min. It was observed that with the progress of time, the SPR peak observed at 580 nm was increased with the increase in the reaction time. Nevertheless, the small red-shift observed at 90 min may be attributed to the formation of larger Cu-NPs. As compared with the UV-vis spectrum of the pure Cu sample, a slight blue shift from 585 to 580 nm was observed for Cu–MoS_2 samples, which could be due to the distribution of smaller Cu-NPs on MoS_2 nanosheets. The presence of Cu-NPs over the MoS_2 nanosheets was analyzed by X-ray diffraction as described in Fig. 2b. Four characteristic peaks of MoS_2 nanosheets appeared at 14.3°, 33.1°, 39.6°, and 58.4°, corresponding well with the (002), (100), (103), and (110) crystal planes (JCPDS card no. 77-1716), respectively. The diffraction peaks for MoS_2 are shown beside the diffraction peaks of Cu at 2θ values of 43.2°, 50.2°, 73.7°, 89.4°, and 94.5°, which were assigned to (111), (200), (220), (311), and (222) reflections of the face-centred-cubic (fcc) structure of the metallic copper, respectively (JCPDS card no. 04-0836). The absorption spectra of Cu-NPs, MoS_2 nanosheets, and Cu–MoS_2 nanocomposites are given in Fig. S1.† Four characteristic absorption bands of MoS_2 nanosheets were observed at 679, 628, 465, and 415 were referred to as the A, B, C, and D peaks, respectively. The A and B peaks could be attributed to the characteristic A and B direct excitonic transitions of MoS_2 with the energy split from the valence band spin–orbital coupling.[34] The C and D peaks were assigned to the direct excitonic transition of the M point.[35] There was one observed absorption peak at 580 nm in the spectrum of the Cu sample. For the Cu–MoS_2 nanocomposite sample, in addition to the four characteristic absorption peaks of MoS_2, the appearance of a new peak at 580 nm confirmed the formation of Cu nanoparticles on MoS_2 nanosheets.

The surfaces of Cu-NPs, Cu_2O-NPs, CuO-NPs, and Cu–MoS_2 modified SPEs were analyzed by scanning electron microscopy

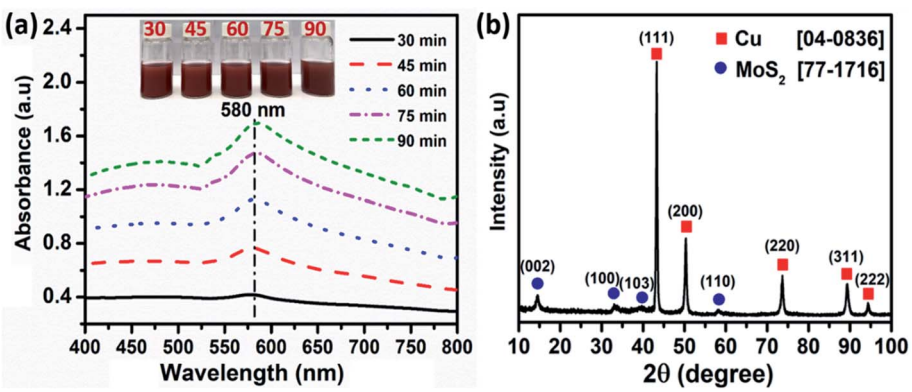

Fig. 2 (a) UV-vis spectra and (b) X-ray diffraction of Cu–MoS_2 nanocomposites. Inset photographs of glass vials of reaction mixtures.

(SEM). All the NMs were decorated on the carbon electrode surface (see Fig. S3†). In the Cu–MoS_2 sample, the synthesized Cu-NPs were tightly and seamlessly enclosed by MoS_2 nanosheets, implying that the appearance of sheet structures like MoS_2 generated good connectivity to the formed Cu-NPs. By stacking 0D (Cu-NPs) and 2D (MoS_2 nanosheets) materials through non-covalent van der Waals interactions, which do not exhibit any additional chemical states besides the metallic contact metal and bulk Mo and S states in MoS_2,[36] homogeneous Cu–MoS_2 heterostructures were prepared. The Cu nuclei with a strong affinity towards valency-deficient S atoms were preferentially anchored to the edges and defects of the MoS_2 nanosheets, where S atoms act as sites for metal nuclei seeding and their subsequent growth into bigger nanostructures *via* Cu(0) crystal-incorporation.[37] The uniform distribution of Cu-NPs could improve the conductivity, enhance the electron transfer rate, and expose more active sites to improve the electrochemical sensing performance.

3.2. Electrochemical investigations

3.2.1. Electrode characterization. To further understand how phase composition and copper loading amount affect the CAP electrochemical sensing performance, the electrochemical properties of the modified electrodes were investigated using CV and EIS measurements in 0.1 M KCl containing 5 mM $[Fe(CN)_6]^{3-/4-}$. Fig. 3 shows CV curves of CuO-NPs/SPE, Cu-NPs/SPE, and Cu_2O-NPs/SPE, respectively. A reversible redox peak of $[Fe(CN)_6]^{3-/4-}$ was observed at all modified electrodes, and under the same conditions, the obtained peak current intensities were different for each electrode. The remarkable enhancement of redox peak current was recorded for the Cu_2O-NPs/SPE (126.2 μA), this modified-SPE manifested a higher current as compared to both Cu-NPs/SPE (121.9 μA) and CuO-NPs/SPE (110.8 μA). To further evaluate the enhancement of the current intensity, the electroactive surface area (EASA) value reflecting the total electrochemically active areas of electrodes was determined by the Randles–Sevcik equation as follows (25 °C):[38]

$$I_p = 2.69 \times 10^5 A n^{3/2} D^{1/2} C \nu^{1/2}$$

where I_p (μA) refers to the cathodic and anodic peak current, A (cm^2) is the electroactive surface area of the electrode (EASA), n is the number of electron transfers in the redox reaction, D ($cm^2\ s^{-1}$) is the diffusion coefficient, C (mol cm^{-3}) is the concentration of $[Fe(CN)_6]^{3-/4-}$, and ν ($V\ s^{-1}$) is the scan rate. EASA was estimated from the graphs of cathodic peak current along with $n = 1$, $D = 6.5 \times 10^{-6}$ cm s^{-1}, $C = 5$ mM, $\nu = 0.05$ V s^{-1}, as listed in Table S2.† The active surface areas of the Cu_2O-NPs/SPE (0.375 cm^2) and Cu-NPs/SPE (0.362 cm^2) were 1.14-fold and 1.1-fold that of CuO-NPs/SPE (0.329 cm^2), respectively. The results showed that the crystal structure and phase composition have a strong effect on the electroactivity of the modified electrode. In general, the larger the active surface area, the better the electrocatalytic performance.[38] Cu_2O-NPs possess the most electroactive surface area among the Cu-based NMs; this suggests that the Cu_2O-NPs-modified SPE will exhibit better electrocatalytic performance as compared to the other two modified electrodes.

EIS measurements were also employed to assess the changes in the surface features of the modified electrodes. The impedance spectra were comprised of semicircles in the higher frequency regions that represent electron transfer resistance (R_{ct}) and the linear part in the lower frequency corresponds to the diffusion of ions.[39] Fig. 3b shows the Nyquist plots of CuO-NPs/SPE, Cu-NPs/SPE, and Cu_2O-NPs/SPE in the supporting electrolyte of 0.1 M KCl solution, containing 5 mM $[Fe(CN)_6]^{3-/4-}$ in the frequency range of 50 kHz to 0.01 Hz with 10 mV amplitude of the AC voltage. The Randles circuit was used as a fitting model in the EIS analysis for the interpretation of the impedance spectra (Fig. S4†). R_1 is the solution resistance, which is dependent on the ionic concentration and the electrode area; R_2 is the charge-transfer resistance (R_{ct}), which is inversely proportional to the electron transfer rate, and dependent on the nature and surface properties of modified nanomaterials; C_1 is the double-layer capacitance, which is directly related to the charging and background current; W_1 is the Warburg impedance, which arises from mass-transfer limitations. For faradaic processes, particular importance is given to the R_{ct}.[40] The R_{ct} values of CuO-NPs, Cu-NPs, and Cu_2O-NPs-modified electrodes were 2149, 1642, and 1473 Ω, respectively, meaning that Cu_2O-NPs/SPE has better charge transfer efficiency than CuO-NPs/SPE and Cu-NPs/SPE.

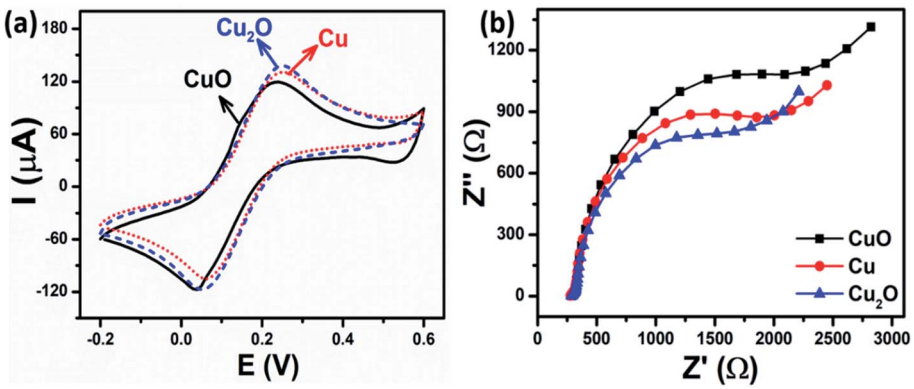

Fig. 3 (a) CV curves and (b) EIS spectra of CuO-NPs, Cu-NPs, and Cu_2O-NPs-modified electrodes in 5 mM $[Fe(CN)_6]^{3-/4-}$ solution containing 0.1 M KCl. The scan rate of CV was 50 mV s^{-1}.

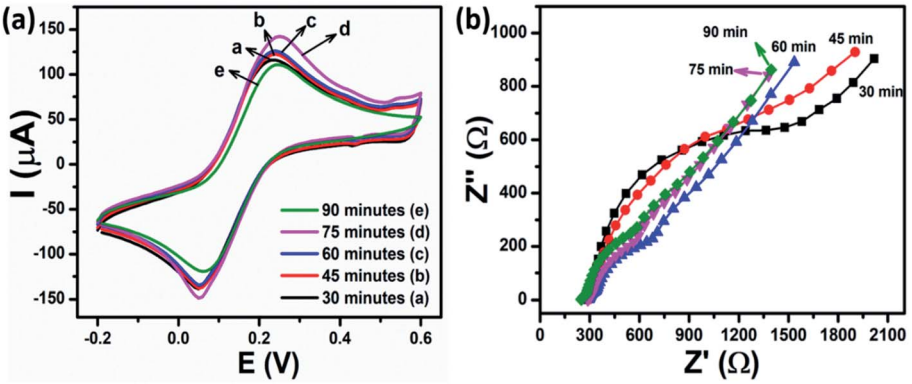

Fig. 4 (a) CV curves and (b) EIS spectra of Cu–MoS_2-modified electrodes synthesized at different reaction times: 30 min, 45 min, 60 min, 75 min, and 90 min in 5 mM $[Fe(CN)_6]^{3-/4-}$ solution containing 0.1 M KCl. The scan rate for CV was 50 mV s^{-1}.

This phenomenon is consistent with the CV results and could be related to the active surface area, electrode transfer, phase composition, as well as crystallinity, and will be discussed in detail below.

The electrochemical properties of the various Cu–MoS_2-modified SPE electrodes were also investigated by CV and EIS techniques. Fig. 4a displays the CV results of five SPE electrodes modified with Cu–MoS_2 nanocomposites and synthesized at different reaction times corresponding to the different copper loading amounts on the surface of MoS_2 nanosheets. Not surprisingly, the current increased with an increase in the amount of Cu-NPs covered on the MoS_2/SPE and reached the maximum at the reaction time of 75 min and then decreased considerably with the extension of the reaction time. The EASA value of the Cu–MoS_2-modified electrodes increased from 0.346 cm^2 to 0.404 cm^2 with the increasing reaction time in the range from 30 min to 75 min. The lower redox peak current, as well as the reduction in the EASA value for Cu–MoS_2-90/SPE, indicated that the electron transfer rate for the $[Fe(CN)_6]^{3-/4-}$ redox process was dramatically decreased. This was caused by the aggregation of Cu-NPs, which decreased the surface area of Cu-NPs and was well in agreement with the UV-vis results.

The electron transfer properties of different Cu–MoS_2-modified electrodes were also investigated by EIS, as shown in Fig. 4b. The R_{ct} values of the Cu–MoS_2-30/SPE, Cu–MoS_2-45/SPE, Cu–MoS_2-60/SPE, Cu–MoS_2-75/SPE, and Cu–MoS_2-90/SPE were 894.7, 674.3, 230.9, 181.8, and 251.3 Ω, respectively. It was noted that the R_{ct} of Cu–MoS_2-75/SPE was smaller than that of all other modified electrodes, which was consistent with the recorded CV curves. More interestingly, the Cu–MoS_2-75/SPE provided a higher EASA value and lower R_{ct} value as compared to the Cu-NPs, Cu_2O-NPs, and even CuO-NPs-modified electrodes. These experimental results suggest that the Cu–MoS_2 nanocomposites possess excellent conductivity due to the synergistic effects of MoS_2 nanosheets and Cu-NPs resulting in the enhancement of the electron transfer ability between the redox probe and the electrode surface.[41]

3.2.2. The effect of Cu-based nanomaterials with tunable phase compositions

3.2.2.1 Effect of tunable phase composition. The electrochemical performances for the detection of CAP on the modified electrodes using Cu-based NMs including Cu-NPs, CuO-NPs, and Cu_2O-NPs were investigated *via* CV measurements in 0.1 M PBS (pH 7.2) containing 50 μM CAP at a scan rate of 60 mV s^{-1}. Fig. 5a shows the electrochemical behavior of the Cu-NPs/SPE-modified electrode in 0.1 M PBS in the absence and the presence of 50 μM CAP. The CV curve of CAP exhibited a sharp

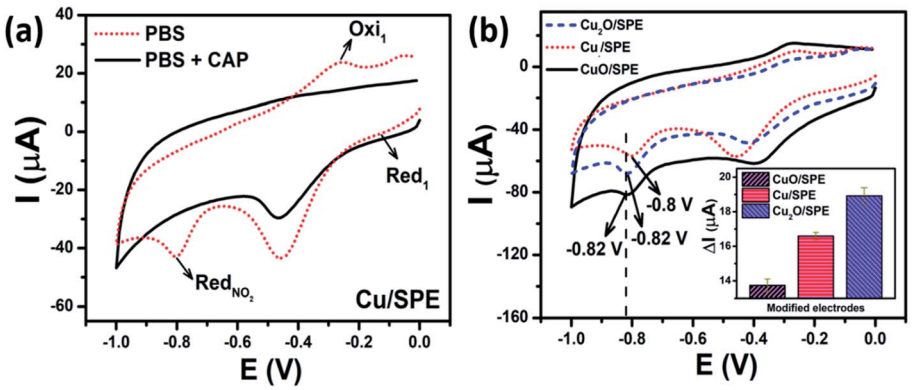

Fig. 5 (a) CV recorded on Cu-NPs/SPE using in 0.1 M PBS (pH 7.2) and PBS (pH 7.2) containing 50 μM CAP. (b) CV curves of CuO-NPs, Cu-NPs, and Cu_2O-NPs-modified electrodes using 0.1 M PBS (pH 7.2) in 50 μM of CAP; the inset shows the corresponding bar chart diagram of irreversible reduction peak current responses for CAP. The scan rate is 60 mV s^{-1}.

and broad irreversible reduction peak at −0.8 V, corresponding to the direct reduction of the nitro group (–NO_2) to hydroxylamine group (–NHOH) in CAP molecules with four electrons (eqn (1)).[42,43] A pair of reversible redox peaks was observed in the potential range of −0.26 V and −0.14 V, corresponding to the reduction of the nitroso derivative into hydroxylamine and *vice versa via* the redox reaction process of the two electrons and two hydrogen ions (eqn (2)). This is consistent with many previous reports for the electrochemical reduction process of CAP occurring at the electrode surface.[38,43–46] In both cases, with and without the presence of CAP, the reduction peak at around −0.4 V to −0.5 V could be ascribed to the irreversible reduction of residual hydroxyl or other functional groups on the commercial SPE surface.[46]

$$R\text{–}NO_2 + 4e^- + 4H^+ \rightarrow R\text{–}NHOH + H_2O\ (Red_{NO_2}) \quad (1)$$

$$R\text{–}NHOH \leftrightarrow R\text{–}NO + 2e^- + 2H^+\ (Oxi_1/Red_1) \quad (2)$$

Fig. 5b shows the CV curves of CuO-NPs, Cu-NPs, and Cu_2O-NPs modified electrodes in 50 μM of CAP and the corresponding bar chart diagram of the irreversible reduction peak current responses for CAP. Two irreversible and sharp reduction peaks were recorded at the CuO-NPs/SPE and Cu_2O-NPs/SPE as the reduction process of CAP at the potential of −0.82 V; meanwhile, for Cu-NPs/SPE, this peak was observed at a lower negative potential value of around −0.8 V. This phenomenon was obvious when comparing the conductivity of a metallic conductor (Cu-NPs) and semiconductors (Cu_2O-NPs and CuO-NPs); Cu-NPs could remarkably promote the electron transfer of CAP on the electrode owing to its excellent electrical conductibility. Nevertheless, the calculated results show that the peak current intensity value for Cu_2O-NPs/SPE was higher as compared CuO-NPs/SPE and Cu-NPs/SPE electrodes (Fig. 5b inset). The utilization of Cu-NPs/SPE enhanced the electronic conductivity, however, it is clear that the electroactive surface area, the adsorption capacity, as well as electrocatalytic efficiency are also important factors affecting the electrochemical performance. These results are consistent with the CV measurements in $[Fe(CN)_6]^{3-/4-}$ and the calculated results for EASA and R_{ct}, showing that the Cu_2O-NPs/SPE exhibited higher sensitivity towards the reduction of CAP. Therefore, all the modified electrodes (*i.e.* CuO-NPs/SPE, Cu-NPs/SPE, and Cu_2O-NPs/SPE) will be further investigated to gain insight into the effect of Cu-based NMs with different phase compositions on the CAP electrochemical sensing performance.

3.2.2.2 The effects of scan rate, pH, and amount of NPs loading on the SPE electrode. The electrochemical behaviors of Cu-NPs- and Cu_2O-NPs-modified electrodes were examined by CV in 0.1 M PBS containing 50 μM of CAP by applying various scan rates from 10 to 60 mV s^{-1} (Fig. S5(a and b)†). It was seen that at both electrodes, the increase in scan rate resulted in increases in the anodic and cathodic peak currents. Furthermore, the cathodic peak potential of CAP slightly shifted to the negative potential side when the scan rate increased. The shifting of the cathodic peak potential of CAP towards the negative direction is due to a decrease in the size of the diffusion layer at faster scan rates.[38] The calibration plots were drawn between the irreversible reduction peak current of CAP *versus* the scan rate of Cu_2O-NPs/SPE, Cu-NPs/SPE, were shown in Fig. S5(d and e),† respectively. The plot of peak current *versus* scan rate presented a good level of linearity, corresponding to the linear regression equations: I_{pc} (μA) = 0.281ν (mV s^{-1}) + 2.153 (R^2 = 0.99) (Cu_2O-NPs/SPE); I_{pc} (μA) = 0.229ν (mV s^{-1}) + 2.468 (R^2 = 0.99) (Cu-NPs/SPE). This implies that the electrochemical behaviors of Cu-NPs and Cu_2O-NPs-modified SPEs were adsorption-controlled processes, not diffusion-controlled processes towards CAP.[38,47]

The buffer pH value is one of the vital parameters that significantly affect the activity of the electrochemical sensor.[48] The influence of buffer pH on the electrochemical responses of Cu-NPs/SPE and Cu_2O-NPs/SPE towards 50 μM CAP in the 0.1 M PBS was investigated in the range from pH 3 to pH 11, as shown in Fig. S6.† The DPV curves revealed that the reduction peak potential of CAP was shifted to negative potential with increasing the pH value. As can be observed, the reduction peak current of CAP increased as the pH increased from 3 to 5, and the highest peak current was seen at pH 5 for all electrodes. The decreases in the peak current beyond pH 5 were recorded. Furthermore, plot of peak potential *versus* pH presented a good level of linearity, corresponding to the linear regression equations: E_{pa} (V) = −0.0266pH − 0.4172 (R^2 = 0.996) (Cu_2O-NPs/SPE); E_{pa} (V) = −0.0318pH − 0.4012 (R^2 = 0.997) (Cu-NPs/SPE). Hence, pH 5 was chosen as the optimized pH for further electrochemical measurements of CuO-NPs, Cu-NPs, and Cu_2O-NPs-modified SPEs. The values of the slope of −31.8 mV pH^{-1} and −26.6 mV pH^{-1} were different from the value −59 mV pH^{-1} for the reversible case, indicating the irreversibility of the peaks.

To optimize the conditions for the loading of functional NMs on the SPEs, the electrochemical response of Cu_2O-NPs/SPE and Cu-NPs/SPE with the various volumes from 2 to 10 μL were conducted by using the DPV technique in the 0.1 M PBS containing 50 μM CAP at a scan rate of 6 mV s^{-1} (see Fig. S7(a and b)†). For the modified electrodes, the reduction peak currents of CAP increased significantly with increasing the modifier amount up to 6 μL. The peak current gradually decreased with further increases in the modifier amount. Hence, similar to the pH parameters, the most appropriate loading amount was chosen as 6 μL for CuO-NPs/SPE, Cu-NPs/SPE, and Cu_2O-NPs/SPE for further electrochemical experiments of CAP detection.

3.2.2.3 Calibration curve. DPV is a differential technique that is immune to residual current and can be used to detect and quantify the analytes at trace levels in analytical applications.[43] Thus, DPV was used to determine the sensitivity, linear concentration range, and limit of detection towards CAP. Fig. 6a–c show the DPV curves of the different CAP concentrations on CuO-NPs/SPE, Cu-NPs/SPE, and Cu_2O-NPs/SPE under the optimized experimental conditions, respectively. As can be observed, when the concentration of the CAP increased, the peak currents also increased and their potentials slightly shifted to the more negative values at all three modified electrodes. This phenomenon could be attributed to the involvement of protons and the change in the pH value around the electrode interface. The H^+ concentration is considered as the major

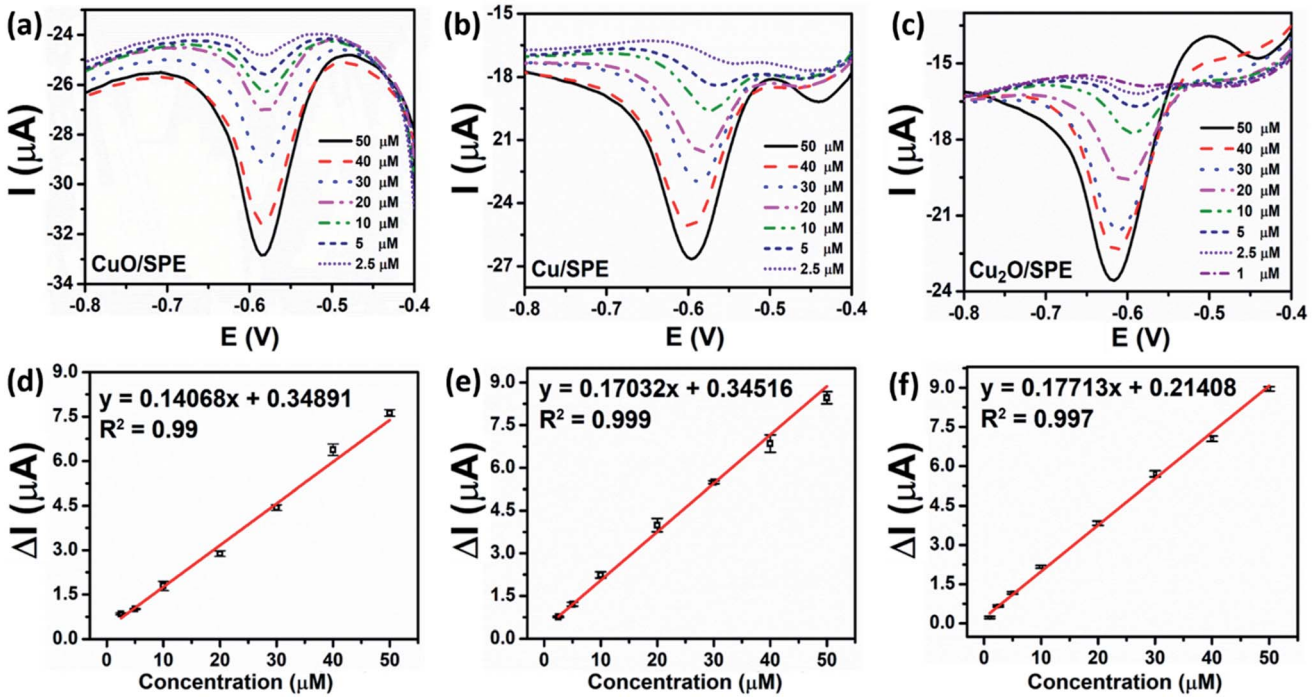

Fig. 6 DPV curves of CuO-NPs/SPE (a), Cu-NPs/SPE (b), and Cu_2O-NPs/SPE (c) in 0.1 M PBS (pH 5) containing CAP (1–50 μM) at a scan rate of 6 mV s^{-1}, corresponding to the calibration plots between peak current *vs.* various concentrations of CAP (d–f), along with error bars.

cause of a decrease in the vicinity of the working electrode, and leads to a slight shift in the peak potential of CAP.[43] In particular, the lowest detectable CAP concentration, sensitivity, repeatability, as well as LOD were different for the different modified electrodes, as shown in Table 1. Both CuO-NPs/SPE and Cu-NPs/SPE exhibited linear ranges in the concentration range of 2.5 to 50 μM, while Cu_2O-NPs/SPE with the higher electroactive surface area (higher EASA value) and the electron transfer enhancement (lower R_{ct}) showed a wider linear range in the concentration range of 1 to 50 μM. Accordingly, the calibration plots were constructed using the DPV peak current response, as shown in Fig. 6d–f corresponding to CuO-NPs/SPE, Cu-NPs/SPE, and Cu_2O-NPs/SPE with the coefficient of correlation R^2 being more than 0.99. The electrochemical sensitivities of CuO-NPs/SPE and Cu-NPs/SPE towards the reduction of CAP were calculated to be 0.141 μA μM^{-1} and 0.17 μA μM^{-1}, respectively; the limits of detection (LOD) were determined to be 0.45 μM and 0.25 μM, respectively, using the standard formula: LOD = $3S_D/S$ (where S_D is the standard deviation, S is the slope value). Notably, the Cu_2O-NPs/SPE exhibited the highest sensitivity towards the reduction of CAP at 0.177 μA μM^{-1}, and the LOD was estimated to be 0.23 μM. The Cu_2O-NPs/SPE achieved a wider linear range, lower detection limit, and better electrochemical sensitivity for the determination of CAP than CuO-NPs/SPE and Cu-NPs/SPE because of the remarkable improvement in the electron transfer through the interface of the electrode/electrolyte solution and its benefit in the electrochemical reduction of CAP. The obtained results show that the crystal phase could significantly affect the electrode processes, which was a critical factor for improving the sensing performance.

3.2.3. The effect of copper loading amount on the performance of the Cu–MoS_2 nanocomposites-based electrochemical sensor

3.2.3.1 The effect of copper loading amount on the surface of MoS_2 nanosheets. The electrochemical responses of modified and un-modified SPEs for CAP were determined by CV. Fig. 7a shows the electrochemical behavior of CAP on the bare SPE and different modified electrodes such as Cu-NPs/SPE and Cu–MoS_2/SPE in 0.1 M PBS (pH 7.2) at a scan rate of 60 mV s^{-1} containing 50 μM CAP. The reduction peak potentials of CAP at the bare SPE and Cu-NPs/SPE electrodes were measured to be −0.795 V and −0.8 V, slowly shifting to the more negative

Table 1 A comparison of the characteristic parameters of CAP electrochemical sensors using CuO-NPs/SPE, Cu-NPs/SPE, and Cu_2O-NPs/SPE

Modified electrodes	EASA (cm^2)	R_{ct} (Ω)	Sensitivity (μA μM^{-1})	Linear range (μM)	LOD (μM)
CuO-NPs	0.329	2149	0.141	2.5–50	0.45
Cu-NPs	0.362	1642	0.17	2.5–50	0.25
Cu_2O-NPs	0.375	1473	0.177	1–50	0.23

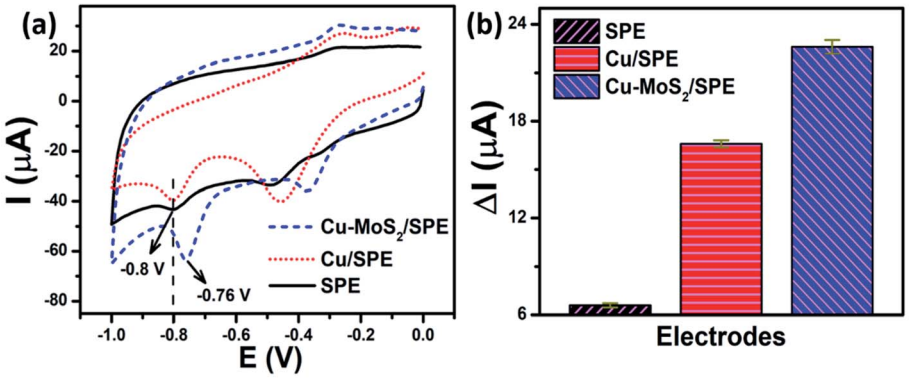

Fig. 7 (a) CV responses at the bare SPE, Cu-NPs/SPE, and Cu–MoS_2/SPE in 0.1 M PBS (pH 7.2) containing 50 μM CAP, and (b) the corresponding bar chart diagram of irreversible reduction peak current responses for CAP. The scan rate is 60 mV s^{-1}.

potential range. The Cu-NPs/SPE offered a higher peak current as compared to the bare SPE, which was attributed to the excellent electrical conductivity of copper, especially at the nanoscale. More interestingly, Cu-NPs in combination with MoS_2 to modify SPE showed the highest peak current at the lowest negative potential of −0.76 V. Furthermore, the reduction peak current response of CAP at Cu–MoS_2/SPE (22.6 μA) was 1.36-fold and 3.42-fold higher as compared to Cu-NPs/SPE (16.6 μA) and bare SPE (6.6 μA), respectively. The shift of the anodic peak to a more negative potential and a higher current response revealed that the Cu–MoS_2/SPE was an effective promoter to enhance the kinetics of the electrochemical process of CAP, suggesting the pronounced electrocatalytic activity of these nanocomposites for the CAP reduction. MoS_2 is known as a material with excellent electrocatalytic activity, however, the poor electrical conductivity significantly restricts its applications.[43] Meanwhile, Cu-NPs are an outstanding conductive nanomaterial. The combination of MoS_2 and Cu-NPs could take their inherent advantages in their properties to enhance the adsorption capacity, conductivity, as well as electrocatalytic activity, resulting in performance improvement in the determination of CAP.

To investigate the effect of the copper loading amount on MoS_2 nanosheets on the CAP electrochemical sensing performance, the CAP electrochemical responses of SPEs modified with Cu–MoS_2 nanocomposites synthesized at various reaction times were considered. In the electrochemical synthesis method, the increase in the reaction time was similar to that of the increase in the copper coating amount on the MoS_2 nanosheets. The influence of the copper loading amount on MoS_2 nanosheets on the current and potential of the reduction peak of CAP is displayed in Fig. 8a. With the progress of reaction time, more and more Cu-NPs were formed, resulting in a remarkable change in the peak potential value as well as peak current. As described in Fig. 8b, the calculated results show that the peak current rapidly increased as the reaction time increased and reached a maximum after 75 min. Unfortunately, the current response of CAP decreased with a further increase in the copper loading amount. To explain this, when the reaction time reached 90 minutes, the greater agglomeration of the formed Cu-NPs on MoS_2 nanosheets led to a decrease in active sites and lower electron transfer within the electrode. This not only reduced detection performance but also led to the easy peeling of the electrode surface during operation. These results were consistent with the UV-vis results and CV measurements in $[Fe(CN)_6]^{3-/4-}$, corresponding to the calculated results for EASA values and EIS spectra. This implies that the synergistic effect of MoS_2 nanosheets with the large surface area, excellent

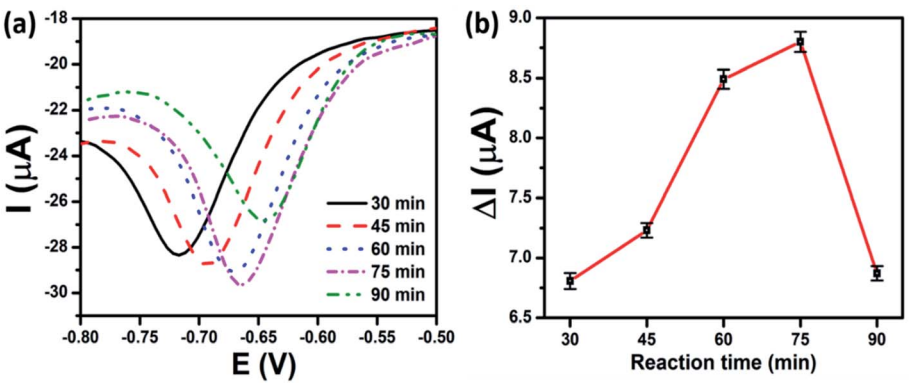

Fig. 8 DPVs recorded on Cu–MoS_2 modified electrodes with various reaction times using in 0.1 M PBS (pH 7.2) containing 50 μM CAP (a); the plots of peak current *vs.* reaction time (b) with error bars. The scan rate is 6 mV s^{-1}.

electrocatalytic activity and Cu-NPs with wonderful electrical conductivity resulted in enhanced electrochemical performance. The results also show that the rational design of the copper loading amount on the MoS_2 nanosheets was critical to the electrochemical activity of Cu–MoS_2 nanocomposites.

3.2.3.2 The effects of scan rate, pH, and amount of nanocomposites on the SPE electrode. The effect of scan rate on Cu–MoS_2-75-modified SPE towards CAP was examined by CV in 0.1 M PBS (pH 7.2) containing 50 μM of CAP by applying various scan rates from 10 to 60 mV s^{-1} (Fig. S5(c)†). It was observed that the reduction peak of CAP slightly shifted to the negative potential side and the peak current increased linearly as the scan rate increased. The calibration plot between reduction peak current and scan rate is shown in Fig. S5(f).† The linear regression equation of I_{pc} (μA) = 0.355ν (mV s^{-1}) + 1.079 (μA) with correlation coefficient of R^2 = 0.984 suggests that the electrochemical reduction of CAP at the Cu–MoS_2-75-modified SPE was an adsorption-controlled process.

The influence of pH value on the electrochemical response of CAP at Cu–MoS_2-75/SPE was investigated in the range of pH 3–11 (Fig. S6(c)†). The DPV curves indicated that the peak potential shifted towards the negative direction when the pH increased from 3 to 11. As shown in Fig. S6(f),† the CAP reduction peak current increased as the pH increased from 3 to 5 and then progressively decreased as the pH of the solution increased. The suitable value of pH 5 was chosen to obtain the highest current in the further electrochemical measurement of CAP. The plot between different pH and peak potentials exhibited good linearity (R^2 = 0.998), with the regression equation of E_{pa} (V) = −0.0324pH − 0.3618. The value of the slope of −32.4 mV pH^{-1} was different from the value −59 mV pH^{-1} for the reversible case, showing the irreversibility of the peaks.

We have investigated the optimized conditions of the loading amounts of Cu–MoS_2-75 nanocomposites on SPE with various volumes from 2 to 10 μL (Fig. S7(c)†). The calculated results show that the current response of CAP rapidly increased with increasing the modifier amounts of Cu–MoS_2-75 nanocomposites and reached a maximum of 6 μL. The reason could be that the superfluous Cu–MoS_2 was densely packed, leading to the formation of a thick film on the electrode, hindering the electron transfer. Therefore, we chose 6 μL of Cu–MoS_2-75 as the optimum modifier amount to investigate their electrochemical performance for CAP detection in more detail.

3.2.3.3 Calibration curve. Under optimum conditions, the quantitative electrochemical detection of CAP by the as-prepared Cu–MoS_2 was conducted *via* DPV measurements as shown in Fig. 9a. As can be observed, the cathodic peak current of CAP was increased with the increasing concentration of CAP in the range from 0.5 to 50 μM. The reduction peak current was linearly proportional to the CAP concentration with correlation coefficient R^2 = 0.99 (Fig. 9b). The electrochemical sensitivity of Cu–MoS_2-75/SPE was calculated to be about 1.74 μA μM^{-1} cm^{-2} and the detection limit was estimated to be 0.19 μM. When comparing the characteristic parameters of these electrochemical sensors, the Cu–MoS_2-75/SPE achieved lower detectable concentration, lower LOD, and better sensitivity for the determination of CAP than CuO-NPs/SPE, Cu_2O-NPs/SPE, and Cu-NPs/SPE. The reason might be that the employment of Cu–MoS_2 nanocomposites could significantly increase the adsorption efficiency, electrical conductivity, and the effective surface area of the SPE electrodes. These results were consistent with the calculated results for EASA and R_{ct} values, which was due to the excellent synergistic effect of the nanocomposites such as a better voltammetric response, high active surface area, and enhanced electron transfer, as well as good electrocatalytic activity.[49,50]

3.2.4. Selectivity, repeatability, stability studies, and real sample analysis of the proposed electrochemical sensors. The selectivity of the developed sensors was examined by the simultaneous addition of possible interfering compounds and ions such as glucose, ascorbic acid, 4-nitrophenol, amoxicillin (AMX), K^+, Na^+, Ni^{2+}, Fe^{3+}, Zn^{2+}, Ag^-, Cl^-, and NO_3^- to a 50 μM CAP standard solution. The tested results are given as a bar chart diagram in Fig. S8.† As shown in the figure, all three modified electrodes have delivered excellent current responses towards CAP in the presence of interfering substances at 10-fold concentrations, except for AMX. The reduction peak potential of CAP remained, while AMX showed 17, 22, and 23% of signals

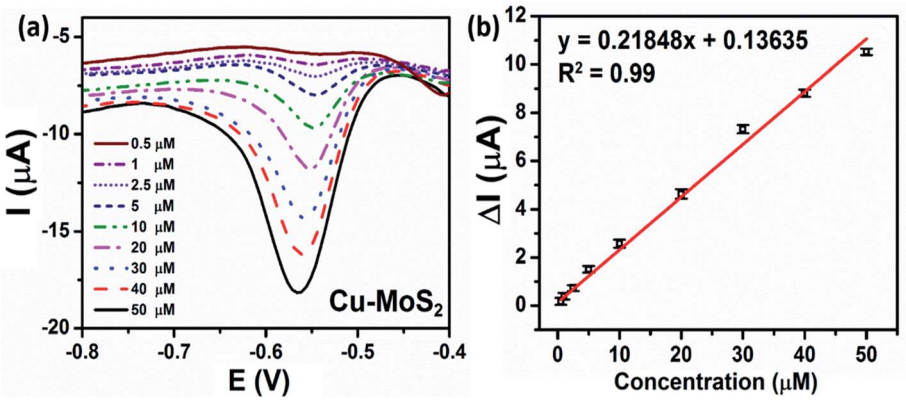

Fig. 9 (a) DPV curves of Cu–MoS_2-75/SPE in 0.1 M PBS (pH 5) containing CAP (0.5–50 μM) at a scan rate of 6 mV s^{-1} corresponding to the calibration plots of the peak current *vs.* various concentrations of CAP (b) along with error bars.

Table 2 Analysis of CAP in honey and milk samples using Cu_2O-NPs, Cu-NPs, and Cu–MoS_2-modified electrodes as electrochemical sensors ($n = 3$)

Electrodes	Sample	Spiked (μM)	Found (μM)	Recovery (%)	RSD (%)[n]
Cu_2O	Honey	5	4.3	85.6	3.1
		10	9.7	97	3
		20	19.1	95.7	3.7
	Milk	5	4.9	97.8	3.5
		10	9.5	95.1	2.3
		20	19.7	98.3	1.2
Cu	Honey	5	4.6	92.9	4.1
		10	9.5	95	1.8
		20	19.8	98.8	4.6
	Milk	5	4.7	94.3	5.4
		10	9.6	96.2	1.1
		20	19.9	99.5	4
Cu–MoS_2	Honey	5	4.9	97.5	2.2
		10	9.9	99	3.4
		20	19.8	98.7	3.3
	Milk	5	5.1	101.4	3.3
		10	10.2	102.4	3.0
		20	20.22	101.1	3.3

(percentage concerning CAP signal) for Cu_2O-NPs/SPE, Cu-NPs/SPE, and Cu–MoS_2-75/SPE, respectively. This is mainly due to the high affinity of sulfur atoms for copper, as well as the chelation between the copper atom and the N atoms from the amino group of AMX,[51,52] which could cause the changes in the effective surface area of the Cu-based NMs-modified electrodes. Therefore, AMX and structurally similar compounds such as ampicillin, penicillin G, ceftazidime, cefadroxil, cefuroxime, *etc.*, may influence the CAP analytical performance of Cu-based electrochemical sensors. Thus, AMX should be separated before the detection of CAP for quantitative analytical purposes, and for rapid and on-site detection, the interference of AMX could be overlooked.

In order to study the repeatability of the modified electrodes, ten repeated DPV measurements were performed towards the determination of CAP (40 μM) on the same electrode under the same conditions (Fig. S9†). The reduction current for CAP at Cu_2O-NPs/SPE, Cu-NPs/SPE, and Cu–MoS_2-75/SPE showed appreciable repeatability with relative standard deviation (RSD) values of 0.31, 0.24, and 0.19%, respectively. The long-term storage stability of the modified electrodes was also investigated by evaluating their responses to the CAP reduction after storage for 14 and 30 days at room temperature. As can be seen in Fig. S10,† the Cu-NPs/SPE, CuO-NPs/SPE, and Cu–MoS_2/SPE still retained 83.4, 86, and 89.6% of their initial current responses after being stored for 30 days, respectively, indicating the capability for long-term storage and the operational stability of the proposed sensors. Unfortunately, it should be emphasized that for the Cu_2O-NPs-modified electrode, the current response retained only 70.8% of its initial response after 30 days. The major decline of the initial reduction current of Cu_2O-NPs/SPE can be mainly attributed to the susceptibility to oxidation of Cu_2O; accordingly, further research is needed to enhance the stability of the electrode after working for 1 month.

The practical feasibilities of the developed electrochemical sensors were investigated for the determination of certain concentrations of CAP in food samples, including milk and honey samples. The spiked CAP concentrations were 5, 10, and 20 μM. According to the obtained DPV curves, the ultimate concentration of CAP was calculated following the regression equation of the calibration curves. The obtained results are summarized in Table 2. For the Cu_2O-NPs/SPE and Cu-NPs/SPE, the average recoveries were in the range of 85.6% to 98.3%, and 92.9% to 99.5%, with the RSD values within 3.7% and 5.4%, respectively ($n = 3$). In contrast, Cu–MoS_2/SPE exhibited greater accuracy and stability with the average recoveries in the range from 98.7% to 102.4%, and the RSD was less than 3.3%. These results demonstrate that the developed electrochemical sensors using Cu_2O-NPs, Cu-NPs, and Cu–MoS_2 nanocomposites had good practical applicability for CAP determination in milk and honey samples.

3.3. Discussion

For the nanostructured electrochemical sensors, the rational design of NMs plays an important role in improving the

Table 3 Comparative study of the performance of various modified electrodes for CAP electrochemical detection[a]

Modified electrodes	Techniques	Analytical ranges (μM)	Limit of detection (μM)	Ref.
Co_3O_4@rGO/GCE	DPV	2–2000	1.16	44
Sr–ZnO@rGO/SPE	LSV	0.19–2847.3	0.131	63
Fe_3O_4–CMC@AuNPs/GCE	SWV	2.5–25	0.066	64
CuNPs@CNTs/MIP/GCE	CV	10–500	10	65
AuNPs–N doped graphene/GCE	LSV	2–80	0.59	47
AuNPs–GO/GCE	Amperometry	1.5–2.95	0.25	48
MoS_2/polyaniline/CPE	DPV	0.1–1000	0.065	66
MoS_2–GO/SPE	DPV	0.1–50	0.05	43
CuO/SPE	DPV	1–50	0.45	This work
Cu_2O/SPE	DPV	1–50	0.23	
Cu/SPE	DPV	2.5–50	0.25	
CuNPs–MoS_2/SPE	DPV	0.5–50	0.19	

[a] SWV: square-wave voltammograms; GCE: glassy carbon electrode; MIP: molecularly imprinted polymer; LSV: linear sweep voltammetry; CPE: carbon paste electrode.

analytical performance of electrochemical sensors. From the perspective of the structure–property–performance relationships, the analytical performance of electrochemical sensors using NMs can be controlled by changing the factors that decisively affect their conductivity, electrocatalytic activity, and adsorption efficiency, such as structure morphology, dimensionality, crystal phase, and composition. In this study, three Cu-based NMs, including CuO-NPs, Cu-NPs, and Cu_2O-NPs, were designed to investigate the roles of copper phase composition on the electrochemical sensing performance of CAP. The orders of the EASA values and R_{ct} values were Cu_2O-NPs/SPE > Cu-NPs/SPE > CuO-NPs/SPE and Cu_2O-NPs/SPE < Cu-NPs/SPE < CuO-NPs/SPE, respectively. Generally, a higher electroactive surface area leads to a better adsorption efficiency and is vital for enhancing the electrochemical performance. Cu_2O-NPs/SPE showed enhanced electrochemical activity due to abundantly available adsorption and/or deposition sites, good electron transfer through the interface of electrode/electrolyte solution, facilitating the charge transferability to the analyte. This can be explained in terms of phase purity, crystallinity, and resistivity. Both CuO and Cu_2O are p-type semiconductors, thus the conduction arises from the presence of holes in the valence band.[53,54] However, unlike CuO, the top states of the valence band in Cu_2O-NPs are derived from the fully occupied Cu $3d^{10}$ states, which are not localized (more mobile) when converted into holes.[55] The formation of Cu vacancies is an often-stated mechanism for the origin of p-type conductivity in Cu_2O-NPs; the hole carriers in Cu_2O-NPs crystalline structures are generated by Cu-vacancies.[54,56,57] Some reports have also studied the effects of phase composition and crystallinity on the resistivity of different types of copper oxide. Figueiredo *et al.*[58] observed that during the conversion from Cu_2O to CuO, the formation of the mixed Cu_2O–CuO phase was accompanied by an increase in resistivity. Recently, Valladares *et al.*[59] reported a difference in the resistivity of the samples with the coexistence of CuO and Cu_2O phases. The authors indicated that in the sample with the dominant CuO phase containing a small amount of Cu_2O, the CuO sites probably acted as electrically neutral defects, which replaced the electrically active Cu vacancies, resulting in the increased electrical resistivity.[60] These results were suitable for the obtained experimental results in our report observed for the CuO sample; the coexistence of the side Cu_2O phase was observed from the XRD pattern, which significantly decreased its electrical conductivity, leading to reduced electrochemical performance. From the XRD and electrochemical analysis results, it can be seen that the single-phase feature with the high crystallinity of Cu and Cu_2O was the major cause of a decrease in the resistivity, suggesting that crystallization might also contribute to the electrical characteristics of the modified electrode. The positive impacts of single-phase Cu and Cu_2O NMs on conductivity are in good agreement with the electrical behaviors of copper and copper oxide reported by other authors.[58–60] Moreover, Cu_2O-NPs with Cu^+ ion centers can effectively catalyze the reduction of antibiotics.[18] Based on the obtained electrochemical results, we found that the phase composition and crystallinity of these Cu-based NMs strongly affected the electron transfer, which were critical factors in improving the CAP electrochemical sensing performance.

The many previous studies indicated that the nanohybrids/nanocomposites exhibited synergistic effects, which not only resolved the drawbacks of the single component but also resulted in better performance.[41] There are two main disadvantages to the practical application of pure MoS_2 like poor charge mobility and low activity, which are attributed to strong van der Waals interactions existing among the lamellar crystals and the relatively low electronic conductivity between two adjacent S–Mo–S layers.[49,61] However, the defects and edges on MoS_2 containing partially unbound sulfur can act as decorated sites for supporting metal NPs,[37] thus achieving amplified signals and increasing the performance of electrochemical sensors.[50,62] The hybrid of Cu-NPs and MoS_2 nanosheets can improve the electroactive surface area, and prevent the oxidation and self-agglomeration of Cu-NPs. Accordingly, the EASA value of

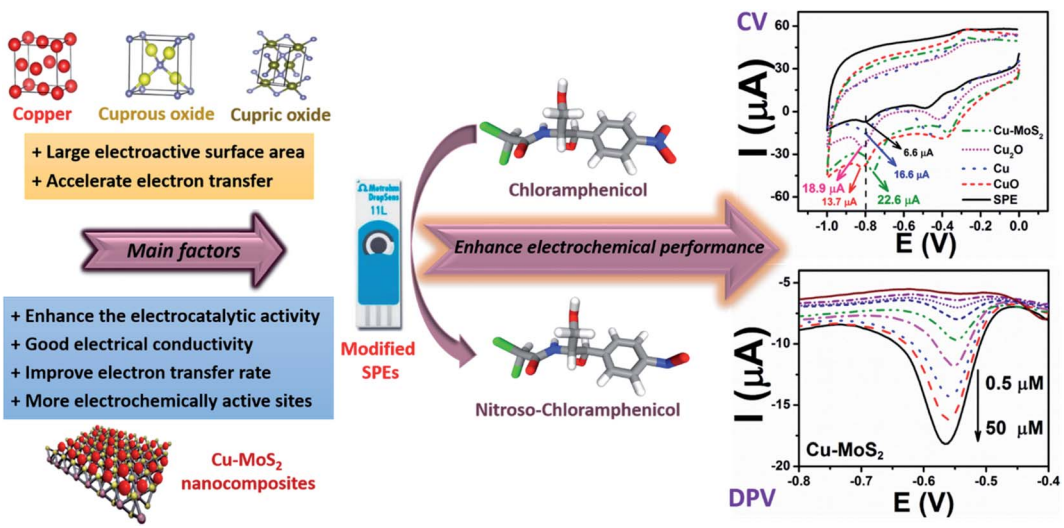

Fig. 10 The proposed mechanism of the electrochemical sensing performance for CAP using SPE electrode modified with Cu-based NMs such as CuO-NPs, Cu-NPs, Cu_2O-NPs, and Cu–MoS_2 nanocomposites.

Cu–MoS_2/SPE was higher than that of Cu_2O-NPs/SPE, Cu-NPs/SPE, and CuO-NPs/SPE. As a result, Cu–MoS_2-modified electrodes exhibited a wider linear range (lower detectable concentration), a lower limit of detection, and better sensitivity for the determination of CAP than Cu_2O-NPs/SPE, Cu-NPs/SPE, and CuO-NPs/SPE. The changes in the copper loading amount on the MoS_2 nanosheets directly varied the electronic and surface properties of Cu–MoS_2 nanocomposites, which strongly affected the electrode processes. The rational design of Cu-NPs amount on the MoS_2 nanosheets significantly reduced the charge transfer resistance and thus improved the electron transfer, which helped to enhance the electrochemical response and lower the detection limit. Our results also suggested that the combination of the advantageous characteristics of MoS_2 and Cu-NPs provided more electroactive sites, facilitated the electron transfer, and enhanced the absorption of CAP on the electrode surface, resulting in the improvement of the electrochemical sensing performance of CAP. The comparison of the analytical parameters of our proposed sensors with various electrochemical sensors for the CAP detection is summarized in Table 3, which indicated that the Cu–MoS_2/SPE afforded good sensitivity and reliability with wide detection ranges. These results show that the proposed electrochemical sensors are suitable and economically efficient for the analysis of CAP, as well as other antibiotics in food samples (Fig. 10).

4. Conclusions

We have demonstrated the effects of phase composition and copper loading amount on the MoS_2 nanosheets on the CAP analytical performance of Cu–MoS_2 nanocomposites-based electrochemical sensors. Electrochemical performance analyses revealed that Cu-NPs and Cu_2O-NPs displayed a higher CAP analytical performance than CuO-NPs in the following order Cu_2O-NPs > Cu-NPs > CuO-NPs. Our results also showed the importance of the rational design of copper loading amount on the MoS_2 nanosheets for the electrochemical response enhancement of CAP (up to ~1.3 times enhancement in the electrochemical response signal). Under optimized conditions, the Cu–MoS_2 nanocomposites-based CAP electrochemical sensor reached an electrochemical sensitivity of 1.74 μA μM^{-1} cm^{-2} with a LOD of 0.19 μM in the detection range from 0.5–50 μM. The designed electrochemical sensor exhibited high stability, satisfactory anti-interference ability, and admirable recovery results in milk and honey analysis. These excellent findings show that Cu–MoS_2 nanocomposites offer great promise for the design and development of high-performance electrochemical sensors to detect residual antibiotics in food samples.

Author contributions

N. T. Anh: investigation, methodology, formal analysis, writing-original draft; N. X. Dinh: conceptualization, validation, investigation, writing-review & editing; T. N. Pham: writing-review & editing, formal analysis; L. K. Vinh: validation, methodology; L. M. Tung: funding acquisition, methodology, visualization; L. A. Tuan: conceptualization, methodology, supervision, project administration, writing-review & editing.

Conflicts of interest

The authors declare that they have no known competing financial interests or personal relationships that could have appeared to influence the work reported in this paper.

Acknowledgements

This research was supported by the Vietnam National Foundation for Science and Technology Development (NAFOSTED) through a fundamental research project (103.02-2020.68). The authors would like to acknowledge the supports with Electrochemical, Raman, and UV-vis measurements from NEB Lab at the Phenikaa University.

References

1 X. Gan and H. Zhao, Understanding signal amplification strategies of nanostructured electrochemical sensors for environmental pollutants, *Curr. Opin. Electrochem.*, 2019, **17**, 56–64, DOI: 10.1016/j.coelec.2019.04.016.

2 L. Rassaei, F. Marken, M. Sillanpää, M. Amiri, C. M. Cirtiu and M. Sillanpää, Nanoparticles in electrochemical sensors for environmental monitoring, *TrAC, Trends Anal. Chem.*, 2011, **30**(11), 1704–1715, DOI: 10.1016/j.trac.2011.05.009.

3 W. Siangproh, W. Dungchai, P. Rattanarat and O. Chailapakul, Nanoparticle-based electrochemical detection in conventional and miniaturized systems and their bioanalytical applications: a review, *Anal. Chim. Acta*, 2011, **690**(1), 10–25, DOI: 10.1016/j.aca.2011.01.054.

4 Y. Li, Z. Wang, L. Sun, L. Liu, C. Xu and H. Kuang, Nanoparticle-based sensors for food contaminants, *TrAC, Trends Anal. Chem.*, 2019, **113**, 74–83, DOI: 10.1016/j.trac.2019.01.012.

5 C. Yang, M. E. Denno, P. Pyakurel and B. J. Venton, Recent trends in carbon nanomaterial-based electrochemical sensors for biomolecules: a review, *Anal. Chim. Acta*, 2015, **887**, 17–37, DOI: 10.1016/j.aca.2015.05.049.

6 X. Li, J. Ping and Y. Ying, Recent developments in carbon nanomaterial-enabled electrochemical sensors for nitrite detection, *TrAC, Trends Anal. Chem.*, 2019, **113**, 1–12, DOI: 10.1016/j.trac.2019.01.008.

7 F. Garkani Nejad, S. Tajik, H. Beitollahi and I. Sheikhshoaie, Magnetic nanomaterials based electrochemical (bio)sensors for food analysis, *Talanta*, 2021, **228**, 122075, DOI: 10.1016/j.talanta.2020.122075.

8 J.-Y. Huang, T. Bao, T.-X. Hu, W. Wen, X.-H. Zhang and S.-F. Wang, Voltammetric determination of levofloxacin using a glassy carbon electrode modified with poly(o-aminophenol) and graphene quantum dots, *Microchim. Acta*, 2017, **184**(1), 127–135, DOI: 10.1007/s00604-016-1982-5.

9 A. Wong, A. M. Santos, F. H. Cincotto, F. C. Moraes, O. Fatibello-Filho and M. D. P. T. Sotomayor, A new electrochemical platform based on low cost nanomaterials for sensitive detection of the amoxicillin antibiotic in different matrices, *Talanta*, 2020, **206**, 120252, DOI: 10.1016/j.talanta.2019.120252.

10 S. Su, J. Chao, D. Pan, L. Wang and C. Fan, Electrochemical Sensors Using Two-Dimensional Layered Nanomaterials, *Electroanalysis*, 2015, **27**(5), 1062–1072, DOI: 10.1002/elan.201400655.

11 A. Joshi and K.-H. Kim, Recent advances in nanomaterial-based electrochemical detection of antibiotics: challenges and future perspectives, *Biosens. Bioelectron.*, 2020, **153**, 112046, DOI: 10.1016/j.bios.2020.112046.

12 A. Kurniawan, F. Kurniawan, F. Gunawan, S.-H. Chou and M.-J. Wang, Disposable electrochemical sensor based on copper-electrodeposited screen-printed gold electrode and its application in sensing l-cysteine, *Electrochim. Acta*, 2019, **293**, 318–327, DOI: 10.1016/j.electacta.2018.08.140.

13 V. Velusamy, *et al.*, Novel electrochemical synthesis of copper oxide nanoparticles decorated graphene-β-cyclodextrin composite for trace-level detection of antibiotic drug metronidazole, *J. Colloid Interface Sci.*, 2018, **530**, 37–45, DOI: 10.1016/j.jcis.2018.06.056.

14 S. Sun, X. Zhang, Q. Yang, S. Liang, X. Zhang and Z. Yang, Cuprous oxide (Cu_2O) crystals with tailored architectures: a comprehensive review on synthesis, fundamental properties, functional modifications and applications, *Prog. Mater. Sci.*, 2018, **96**, 111–173, DOI: 10.1016/j.pmatsci.2018.03.006.

15 M. Vincent, P. Hartemann and M. Engels-Deutsch, Antimicrobial applications of copper, *Int. J. Hyg. Environ. Health*, 2016, **219**(7), 585–591, DOI: 10.1016/j.ijheh.2016.06.003.

16 H. Bagheri, A. Hajian, M. Rezaei and A. Shirzadmehr, Composite of Cu metal nanoparticles-multiwall carbon nanotubes-reduced graphene oxide as a novel and high performance platform of the electrochemical sensor for simultaneous determination of nitrite and nitrate, *J. Hazard. Mater.*, 2017, **324**, 762–772, DOI: 10.1016/j.jhazmat.2016.11.055.

17 Y. Huang, *et al.*, Stable Copper Nanoparticle Photocatalysts for Selective Epoxidation of Alkenes with Visible Light, *ACS Catal.*, 2017, **7**(8), 4975–4985, DOI: 10.1021/acscatal.7b01180.

18 X. Ma, J. Li, J. Luo, C. Liu and S. Li, Electrochemical sensor for the determination of dimetridazole using a 3D Cu_2O/ErGO-modified electrode, *Anal. Methods*, 2018, **10**(27), 3380–3385, DOI: 10.1039/C8AY00589C.

19 W. Choi, N. Choudhary, G. H. Han, J. Park, D. Akinwande and Y. H. Lee, Recent development of two-dimensional transition metal dichalcogenides and their applications, *Mater. Today*, 2017, **20**(3), 116–130, DOI: 10.1016/j.mattod.2016.10.002.

20 G. S. Papanai, I. Sharma, G. Kedawat and B. K. Gupta, Qualitative Analysis of Mechanically Exfoliated MoS_2 Nanosheets Using Spectroscopic Probes, *J. Phys. Chem. C*, 2019, **123**(44), 27264–27271, DOI: 10.1021/acs.jpcc.9b09191.

21 J. Chen, G.-G. Ying and W.-J. Deng, Antibiotic Residues in Food: Extraction, Analysis, and Human Health Concerns, *J. Agric. Food Chem.*, 2019, **67**(27), 7569–7586, DOI: 10.1021/acs.jafc.9b01334.

22 M. Bacanlı and N. Başaran, Importance of antibiotic residues in animal food, *Food Chem. Toxicol.*, 2019, **125**, 462–466, DOI: 10.1016/j.fct.2019.01.033.

23 H. M. Feder, C. Osier and E. G. Maderazo, Chloramphenicol: a review of its use in clinical practice, *Rev. Infect. Dis.*, 1981, **3**(3), 479–491, DOI: 10.1093/clinids/3.3.479.

24 P. Shukla, F. W. Bansode and R. K. Singh, Chloramphenicol Toxicity: A Review, *Journal of Medicine and Medical Sciences*, 2011, **2**(13), 1313–1316.

25 E. P. on C. in the F. C. (CONTAM), Scientific Opinion on Chloramphenicol in food and feed, *EFSA J.*, 2014, **12**(11), DOI: 10.2903/j.efsa.2014.3907.

26 P. H. Serrano, Responsible use of antibiotics in aquaculture, *FAO Fish. Tech. Pap.*, 2005, **469**, 97.

27 F. A. Akgul, G. Akgul, N. Yildirim, H. E. Unalan and R. Turan, Influence of thermal annealing on microstructural, morphological, optical properties and surface electronic structure of copper oxide thin films, *Mater. Chem. Phys.*, 2014, **147**(3), 987–995, DOI: 10.1016/j.matchemphys.2014.06.047.

28 B. K. Meyer, *et al.*, The Physics of Copper Oxide (Cu_2O), *Semicond. Semimetals*, 2013, **88**, 201–226, DOI: 10.1016/B978-0-12-396489-2.00006-0.

29 G. Prabhakaran and R. Murugan, Room temperature ferromagnetic properties of Cu_2O microcrystals, *J. Alloys Compd.*, 2013, **579**, 572–575, DOI: 10.1016/j.jallcom.2013.07.094.

30 S. Kumar, Influence of synthesis strategy on the formation of microspheres of self-assembled CuO rectangular nanorods and hierarchical structures of self-assembled Cu_2O nanospheres from single precursor (copper (II) acetate monohydrate) and their structural, optica, *Mater. Chem. Phys.*, 2021, **258**(II), 123929, DOI: 10.1016/j.matchemphys.2020.123929.

31 P. Dawson, M. M. Hargreave and G. R. Wilkinson, The dielectric and lattice vibrational spectrum of cuprous oxide, *J. Phys. Chem. Solids*, 1973, **34**(12), 2201–2208.

32 J. Reydellet, M. Balkanski and D. Trivich, Light Scattering and Infrared Absorption in Cuprous Oxide, *Phys. Status Solidi*, 1972, **52**(1), 175–185, DOI: 10.1002/pssb.2220520120.

33 L. Debbichi, M. C. Marco De Lucas, J. F. Pierson and P. Krüger, Vibrational properties of CuO and Cu_4O_3 from first-principles calculations, and Raman and infrared spectroscopy, *J. Phys. Chem. C*, 2012, **116**(18), 10232–10237, DOI: 10.1021/jp303096m.

34 Y. Yao, *et al.*, High-concentration aqueous dispersions of MoS_2, *Adv. Funct. Mater.*, 2013, **23**(28), 3577–3583, DOI: 10.1002/adfm.201201843.

35 E. P. Nguyen, *et al.*, Investigation of two-solvent grinding assisted liquid phase exfoliation of layered MoS Investigation of two-solvent grinding assisted liquid phase exfoliation of layered MoS_2, *Chem. Mater.*, 2015, **27**(1), 53–59.

36 C. M. Smyth, R. Addou, S. McDonnell, C. L. Hinkle and R. M. Wallace, Contact metal-MoS_2 interfacial reactions and potential implications on MoS_2-based device performance, *J. Phys. Chem. C*, 2016, **120**(27), 14719–14729, DOI: 10.1021/acs.jpcc.6b04473.

37 T. S. Sreeprasad, P. Nguyen, N. Kim and V. Berry, Controlled, defect-guided, metal-nanoparticle incorporation onto MoS_2 via chemical and microwave routes: electrical, thermal, and structural properties, *Nano Lett.*, 2013, **13**(9), 4434–4441, DOI: 10.1021/nl402278y.

38 N. Sebastian, W. C. Yu and D. Balram, Electrochemical detection of an antibiotic drug chloramphenicol based on a graphene oxide/hierarchical zinc oxide nanocomposite, *Inorg. Chem. Front.*, 2019, **6**(1), 82–93, DOI: 10.1039/c8qi01000e.

39 T. Kokulnathan, T. S. K. Sharma, S. M. Chen, T. W. Chen and B. Dinesh, Ex situ decoration of graphene oxide with palladium nanoparticles for the highly sensitive and selective electrochemical determination of chloramphenicol in food and biological samples, *J. Taiwan Inst. Chem. Eng.*, 2018, **89**, 26–38, DOI: 10.1016/j.jtice.2018.04.030.

40 J. Muñoz, R. Montes and M. Baeza, Trends in electrochemical impedance spectroscopy involving nanocomposite transducers: characterization, architecture surface and bio-sensing, *TrAC, Trends Anal. Chem.*, 2017, **97**, 201–215, DOI: 10.1016/j.trac.2017.08.012.

41 S. Su, *et al.*, Improving performance of MoS2-based electrochemical sensors by decorating noble metallic nanoparticles on the surface of MoS2 nanosheet, *RSC Adv.*, 2016, **6**(80), 76614–76620, DOI: 10.1039/c6ra12401a.

42 J. Chen, J. Shih, C. Liu, M. Kuo and J. Zen, Disposable Electrochemical Sensor for Determination of Nitroaromatic Compounds by a Single-Run Approach, *Anal. Chem.*, 2006, **78**(11), 3752–3757.

43 N. X. Dinh, *et al.*, Ultrasensitive determination of chloramphenicol in pork and chicken meat samples using a portable electrochemical sensor: effects of 2D nanomaterials on the sensing performance and stability, *New J. Chem.*, 2021, **45**, 7622–7636, DOI: 10.1039/d1nj00582k.

44 M. Yadav, V. Ganesan, R. Gupta, D. K. Yadav and P. K. Sonkar, Cobalt oxide nanocrystals anchored on graphene sheets for electrochemical determination of chloramphenicol, *Microchem. J.*, 2019, **146**, 881–887, DOI: 10.1016/j.microc.2019.02.025.

45 T. Sun, *et al.*, Electrochemical sensor sensitive detection of chloramphenicol based on ionic-liquid-assisted synthesis of de-layered molybdenum disulfide/graphene oxide nanocomposites, *J. Appl. Electrochem.*, 2019, **49**, 261–270, DOI: 10.1007/s10800-018-1271-6.

46 T. N. Pham, *et al.*, Roles of Phase Purity and Crystallinity on Chloramphenicol Sensing Performance of $CuCo_2O_4$/$CuFe_2O_4$ -based Electrochemical Nanosensors, *J. Electrochem. Soc.*, 2021, **168**(2), 026506, DOI: 10.1149/1945-7111/abde80.

47 J. Borowiec, R. Wang, L. Zhu and J. Zhang, Synthesis of nitrogen-doped graphene nanosheets decorated with gold nanoparticles as an improved sensor for electrochemical determination of chloramphenicol, *Electrochim. Acta*, 2013, **99**, 138–144, DOI: 10.1016/j.electacta.2013.03.092.

48 R. Karthik, *et al.*, Green synthesized gold nanoparticles decorated graphene oxide for sensitive determination of chloramphenicol in milk, powdered milk, honey and eye drops, *J. Colloid Interface Sci.*, 2016, **475**, 46–56, DOI: 10.1016/j.jcis.2016.04.044.

49 F. Li, *et al.*, Synthesis of Cu-MoS_2/rGO hybrid as non-noble metal electrocatalysts for the hydrogen evolution reaction, *J. Power Sources*, 2015, **292**, 15–22, DOI: 10.1016/j.jpowsour.2015.04.173.

50 S. Zhang, Y. Tang, Y. Chen and J. Zheng, Synthesis of gold nanoparticles coated on flower-like MoS_2 microsphere and their application for electrochemical nitrite sensing, *J. Electroanal. Chem.*, 2019, **839**, 195–201, DOI: 10.1016/j.jelechem.2019.03.036.

51 M. Akhond, G. Absalan and H. Ershadifar, Highly sensitive colorimetric determination of amoxicillin in pharmaceutical formulations based on induced aggregation of gold nanoparticles, *Spectrochim. Acta, Part A*, 2015, **143**, 223–229, DOI: 10.1016/j.saa.2015.01.071.

52 R. Zhao, *et al.*, Preparation of phosphorylated polyacrylonitrile-based nanofiber mat and its application for heavy metal ion removal, *Chem. Eng. J.*, 2015, **268**, 290–299, DOI: 10.1016/j.cej.2015.01.061.

53 L. C. Olsen, F. W. Addis and W. Miller, Experimental and theoretical studies of Cu_2O solar cells, *Sol. Cells*, 1982, **7**(3), 247–279, DOI: 10.1016/0379-6787(82)90050-3.

54 A. O. Musa, T. Akomolafe and M. J. Carter, Production of cuprous oxide, a solar cell material, by thermal oxidation and a study of its physical and electrical properties, *Sol. Energy Mater. Sol. Cells*, 1998, **51**(3–4), 305–316, DOI: 10.1016/S0927-0248(97)00233-X.

55 G. A. S. J. Ghisjen, L. H. Tjeng, J. van Elp, H. Eskes, J. Westerink and M. T. Czyzyk, Electronic structure of Cu_2O and CuO, *Phys. Rev. B: Condens. Matter Mater. Phys.*, 1988, **38**(16), 11322–11330, DOI: 10.1103/PhysRevB.38.11322.

56 N. Kikuchi and K. Tonooka, Electrical and structural properties of Ni-doped Cu_2O films prepared by pulsed laser deposition, *Thin Solid Films*, 2005, **486**(1–2), 33–37, DOI: 10.1016/j.tsf.2004.12.044.

57 J. Xue and R. Dieckmann, The non-stoichiometry and the point defect structure of cuprous oxide (Cu_2-δO), *J. Phys. Chem. Solids*, 1990, **51**(11), 1263–1275, DOI: 10.1016/0022-3697(90)90003-X.

58 V. Figueiredo, *et al.*, Effect of post-annealing on the properties of copper oxide thin films obtained from the oxidation of evaporated metallic copper, *Appl. Surf. Sci.*, 2008, **254**(13), 3949–3954, DOI: 10.1016/j.apsusc.2007.12.019.

59 L. De Los Santos Valladares, *et al.*, Crystallization and electrical resistivity of Cu_2O and CuO obtained by thermal oxidation of Cu thin films on SiO_2/Si substrates, *Thin Solid Films*, 2012, **520**(20), 6368–6374, DOI: 10.1016/j.tsf.2012.06.043.

60 V. F. Drobny and L. Pulfrey, Properties of reactively-sputtered copper oxide thin films, *Thin Solid Films*, 1979, **61**(1), 89–98, DOI: 10.1016/0040-6090(79)90504-2.

61 X. Su, Y. Han, Z. Liu, L. Fan and Y. Guo, One-pot synthesized AuNPs/MoS_2/rGO nanocomposite as sensitive electrochemical aptasensing platform for nucleolin

detection, *J. Electroanal. Chem.*, 2020, **859**, 113868, DOI: 10.1016/j.jelechem.2020.113868.

62 J. Zhou, *et al.*, One-step electrodeposition of Au-Pt bimetallic nanoparticles on MoS_2 nanoflowers for hydrogen peroxide enzyme-free electrochemical sensor, *Electrochim. Acta*, 2017, **250**, 152–158, DOI: 10.1016/j.electacta.2017.08.044.

63 S. V. Selvi, N. Nataraj and S. M. Chen, The electro-catalytic activity of nanosphere strontium doped zinc oxide with rGO layers screen-printed carbon electrode for the sensing of chloramphenicol, *Microchem. J.*, 2020, **159**(May), 105580, DOI: 10.1016/j.microc.2020.105580.

64 P. Jakubec, V. Urbanová, Z. Medříková and R. Zbořil, Advanced Sensing of Antibiotics with Magnetic Gold Nanocomposite: Electrochemical Detection of Chloramphenicol, *Chem.–Eur. J.*, 2016, **22**(40), 14279–14284, DOI: 10.1002/chem.201602434.

65 A. Munawar, M. A. Tahir, A. Shaheen, P. A. Lieberzeit, W. S. Khan and S. Z. Bajwa, Investigating nanohybrid material based on 3D CNTs@Cu nanoparticle composite and imprinted polymer for highly selective detection of chloramphenicol, *J. Hazard. Mater.*, 2018, **342**, 96–106, DOI: 10.1016/j.jhazmat.2017.08.014.

66 R. Yang, J. Zhao, M. Chen, T. Yang, S. Luo and K. Jiao, Electrocatalytic determination of chloramphenicol based on molybdenum disulfide nanosheets and self-doped polyaniline, *Talanta*, 2015, **131**, 619–623, DOI: 10.1016/j.talanta.2014.08.035.